Available online at www.sciencedirect.com

ScienceDirect

Journal of Solid State Chemistry 179 (2006) 3489–3499

JOURNAL OF SOLID STATE CHEMISTRY

www.elsevier.com/locate/jssc

# Structure property relationships in the $A\mathrm{Ti_2O_4}$ ($A$ = Na, Ca) family of reduced titanates

Margret J. Geselbracht[a,*], Ann S. Erickson[a], Matthew P. Rogge[a], John E. Greedan[b], Richard I. Walton[c], Matthew W. Stoltzfus[d], Hank W. Eng[d], Patrick M. Woodward[d]

[a] Reed College, 3203 SE Woodstock Blvd. Portland, OR 97202, USA
[b] Brockhouse Institute for Materials Research and Department of Chemistry, McMaster University, Hamilton, Ont., Canada, L8S 4M1
[c] Department of Chemistry, University of Warwick, Coventry, CV4 7AL, UK
[d] Department of Chemistry, Ohio State University, Columbus, OH 43210, USA

Received 20 April 2006; received in revised form 28 June 2006; accepted 7 July 2006
Available online 21 July 2006

## Abstract

Reduced titanates in the $A\mathrm{Ti_2O_4}$ ($A$ = Li, Mg) spinel family exhibit a variety of interesting electronic and magnetic properties, most notably superconductivity in the mixed-valence spinel, $\mathrm{Li_{1+x}Ti_{2-x}O_4}$. The sodium and calcium analogs, $\mathrm{NaTi_2O_4}$ and $\mathrm{CaTi_2O_4}$, each differ in structure, the main features of which are double rutile-type chains composed of edge-sharing $\mathrm{TiO_6}$ octahedra. We report for the first time, the properties and band structures of these two materials. XANES spectroscopy at the Ti K-edge was used to probe the titanium valence. The absorption edge position and the pre-edge spectral features observed in the XANES data confirm the assignment of $\mathrm{Ti^{3+}}$ in $\mathrm{CaTi_2O_4}$ and mixed-valence $\mathrm{Ti^{3+}/Ti^{4+}}$ in $\mathrm{NaTi_2O_4}$. Temperature-dependent resistivity and magnetic susceptibility studies are consistent with the classification of both $\mathrm{NaTi_2O_4}$ and $\mathrm{CaTi_2O_4}$ as small band-gap semiconductors, although changes in the high-temperature magnetic susceptibility of $\mathrm{CaTi_2O_4}$ suggest a possible insulator–metal transition near 700 K. Band structure calculations agree with the observed electronic properties of these materials and indicate that while Ti–Ti bonding is of minimal importance in $\mathrm{NaTi_2O_4}$, the titanium atoms in $\mathrm{CaTi_2O_4}$ are weakly dimerized at room temperature.

*Keywords:* Mixed-valence; Titanate; Xanes spectroscopy; Electronic structure; Band structure; Magnetic susceptibility; Electrical resistivity

## 1. Introduction

Reduced alkali metal and alkaline earth metal titanium oxides exhibit a variety of interesting electronic and magnetic properties and phase transitions [1]. Perhaps best known is the superconducting mixed-valence spinel, $\mathrm{Li_{1+x}Ti_{2-x}O_4}$, with a relatively high $T_c$ (~13 K) for an early transition metal oxide [2]. Substitution of magnesium on the lithium site in $\mathrm{Li_{1-x}Mg_xTi_2O_4}$ suppresses superconductivity [3], while the mixed-valence magnesium titanate spinel, $\mathrm{Mg_{2-x}Ti_{1+x}O_4}$, shows no evidence of superconductivity across the solid solution series [4], despite early, unconfirmed reports of resistivity anomalies. More recently, interest has focused on the properties of the stoichiometric spinel, $\mathrm{MgTi_2O_4}$. In 2002, Isobe and Ueda reported a metal to spin-singlet insulator phase transition at 260 K in $\mathrm{MgTi_2O_4}$ accompanied by a cubic to tetragonal structural transition [5]. Schmidt and coworkers determined the low temperature structure of $\mathrm{MgTi_2O_4}$ and identified Ti–Ti dimers ordered in an unusual helical arrangement; they proposed this dimerization pattern leads to orbital ordering and the opening of a modest gap in the low temperature insulator [6]. Very recently on the basis of thermoelectric power measurements, Zhou and Goodenough reclassified the electronic transition in $\mathrm{MgTi_2O_4}$ as a semiconductor–semiconductor transition associated with dimerization instabilities rather than a classic Peierls transition [7].

Within the $A\mathrm{Ti_2O_4}$ family ($A$ = Li, Mg, Na, Ca) as the $A$ cation becomes too large for the tetrahedral site, the spinel structure is no longer stable, and new structures are

---

*Corresponding author. Fax: +503 788 6643.
*E-mail address:* mgeselbr@reed.edu (M.J. Geselbracht).

0022-4596/$ - see front matter © 2006 Elsevier Inc. All rights reserved.
doi:10.1016/j.jssc.2006.07.024

adopted by the sodium and calcium analogs. $NaTi_2O_4$ crystallizes in a calcium ferrite-type structure in which double rutile-type chains condense through corner-sharing to form one-dimensional tunnels in which the sodium ions are located [8]. $CaTi_2O_4$ adopts a structure that is closely related to $NaTi_2O_4$. The double rutile-type chains are retained, as are the one-dimensional tunnels for the larger $Ca^{2+}$ ions, but in $CaTi_2O_4$ the double rutile-type chains condense through both edge- and corner-sharing. [9] Considering the similar ionic radii of $Na^+$ and $Ca^{2+}$ and the identical stoichiometries of the two compounds it is perhaps surprising that these two compounds are not isostructural. Until now, the difficulties in synthesizing $NaTi_2O_4$ and $CaTi_2O_4$ as originally reported have precluded any study of their properties. However, Geselbracht and coworkers have recently described new synthesis routes to $NaTi_2O_4$ and $CaTi_2O_4$ that allow for the preparation of high-quality samples suitable for further study [9b,10]. In this paper we report for the first time, the properties of these two materials. We have carried out XANES at the Ti K-edge to probe titanium valence. Temperature-dependent resistivity and magnetic susceptibility studies were conducted and informed by band structure calculations in order to better understand structure property relationships in $ATi_2O_4$ ($A = $ Na, Ca). We propose that the dimerization of $Ti^{3+}$ in $CaTi_2O_4$ at room temperature lies behind the subtle structural differences of $NaTi_2O_4$ and $CaTi_2O_4$.

## 2. Experimental methods

Samples of $NaTi_2O_4$ and $CaTi_2O_4$ were prepared as described previously [9b,10]. Phase purity was confirmed by X-ray powder diffraction on a Scintag XDS-2000 diffractometer using Cu$K_\alpha$ radiation. Individual needle-shaped crystals of $NaTi_2O_4$ and $CaTi_2O_4$ were selected for resistivity measurements. The very small size of the crystals (typically, $0.02 \times 0.04 \times 0.4$ mm) limited this study to two-probe measurements. Pt leads were attached to the crystal with silver paint, DuPont Conductor Composition 6838. A Keithley model 617 programmable electrometer was used to measure the resistance. At room temperature, the resistance of the contacts and leads was very small (6–7 Ω) compared to that of a typical crystal (>1000 Ω). Once the leads were attached and the integrity of the contacts was verified, the crystal was covered with Apeizon Type M grease to act as a heat sink and minimize self-heating of the crystal due to the high resistance. Typically, measurements of the resistance were taken every 5 K starting at 300 K and cooling until the resistance of the crystal became too large to measure accurately. Resistivity values were calculated from the resistance and the dimensions of the crystal. Magnetic susceptibility was measured using a Quantum Design MPMS SQUID magnetometer in an applied field of 0.5 T in a helium atmosphere over the temperature range 5–800 K for $CaTi_2O_4$ and 2–600 K for $NaTi_2O_4$. The data above 350 K were obtained using an oven insert.

Titanium K-edge XANES spectra were recorded on Station 7.1 of the Daresbury SRS. The SRS operates with an average stored-energy of 2 GeV and a typical electron-current of 200 mA; Station 7.1 receives X-rays in the 4–10 keV energy range. The station is equipped with a harmonic-rejecting, double-crystal Si(111) monochromator, the second crystal of which allows sagittal focusing of the X-ray beam. Harmonic rejection was set to 50% for all experiments by detuning the second crystal to 50% of the maximum X-ray intensity. Ionization chambers placed before ($I_0$) and behind ($I_t$) the sample and were filled with appropriate quantities of inert gases (Ar–He mixture) to maximize the detection of the X-rays. Data were recorded in transmission mode from samples diluted in polyethylene powder and pressed into self-supporting discs. Dilution was necessary to prevent self-absorption; around 20% sample by mass was used. X-ray energy was scanned with a step size equivalent to at least 0.2 eV. Data were also measured simultaneously from a titanium foil were placed between the second and a third ionization chamber. This allowed accurate energy calibration of the XANES spectra and also provided a check as to the consistency of the data. Data were analyzed using the Daresbury data analysis programs EXCALIB and EXBROOK [11], the former providing the energy calibration and the latter producing normalized XANES spectra with the edge jump determined by normalization to the immediate post-edge background, fitted with a polynomial.

Electronic band structure calculations were carried out using version 47 of the Stuttgart tight bonding, linear muffin tin orbital, atomic sphere approximation (LMTO) code. LMTO is a self-consistent, density functional theory code, which incorporates scalar-relativistic corrections. Detailed descriptions of the ab -initio calculations using the LMTO method are given elsewhere [12,13]. The effects of exchange and correlation were approximated using the Perdew–Wang generalized gradient approximation [14].

## 3. Results and discussion

### 3.1. Structure and valence of $NaTi_2O_4$ and $CaTi_2O_4$

Before describing the band structures and properties of $NaTi_2O_4$ and $CaTi_2O_4$, a brief review of the structural chemistry is useful. $NaTi_2O_4$ crystallizes in an orthorhombic (*Pnam*), calcium ferrite-type structure as shown in Fig. 1a [8]. This structure is built up from double rutile-type chains composed of edge-sharing $TiO_6$ octahedra extending along the *c*-axis. Four neighboring chains condense by corner-sharing to form one-dimensional tunnels containing the sodium cations. There are two crystallographic sites for titanium in this structure, both surrounded by a distorted octahedron of oxygen. The Ti(1) sites are represented in Fig. 1a as light blue Ti(1)$O_6$ octahedra, and the Ti(2)$O_6$ octahedra are shown in medium blue. The non-integer valence of titanium raises the possibility of charge ordering. However, Akimoto and

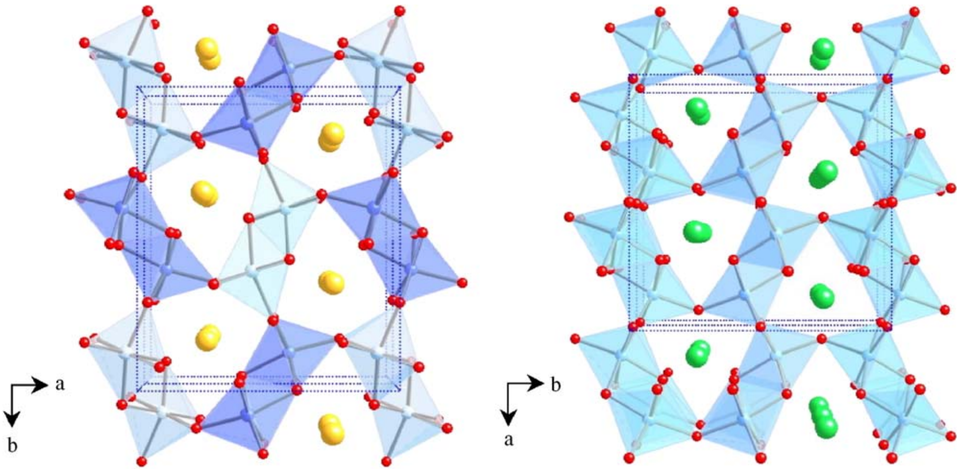

Fig. 1. (a) On the left, the structure of $NaTi_2O_4$ viewed along the *c*-axis. The $Ti(1)O_6$ octahedra are shown in light blue; the $Ti(2)O_6$ octahedra are medium blue. Sodium ions are represented as yellow spheres. (b) On the right, the structure of $CaTi_2O_4$ showing $TiO_6$ octahedra in blue and calcium ions as green spheres.

Takei concluded that the two titanium sites were randomly occupied by $Ti^{3+}$ and $Ti^{4+}$ based on the similar average Ti–O bond distances for each site [8]. The Ti–O bond distances for the Ti(1) site range from 1.932(2) to 2.051(1) Å with an average of 2.026 Å. The Ti–O distances for the Ti(2) site are more similar, ranging from 1.975(2) to 2.020(2) Å with an average of 2.002 Å.

The structure of $CaTi_2O_4$ shares some similarities to that of $NaTi_2O_4$; it is also composed of double rutile-type chains of edge-sharing $TiO_6$ octahedra as shown in Fig. 1b. [9] In $CaTi_2O_4$ (*Bbmm*), the double rutile-type chains, extending along the *c* direction, are joined by additional edge-sharing to form puckered sheets perpendicular to the *b*-axis. These puckered sheets condense by corner-sharing to neighboring sheets, resulting in a pseudo one-dimensional tunnel site for the calcium ions. This arrangement of the double rutile-type chains results in only one crystallographic site for titanium, fully occupied by $Ti^{3+}$. The $TiO_6$ octahedra are distorted with Ti–O bond distances of 1.961(1), 1.974(2), 2.0982(9) (×2), and 2.135(1) Å (×2). The two short Ti–O bonds are *trans*- to each other and not involved in the edge-sharing. Thus, the $TiO_6$ octahedron is compressed perpendicular to the chain direction. It should be noted that the average Ti–O bond distance, 2.067 Å, is longer than either of the averages for the two titanium sites in $NaTi_2O_4$, consistent with the lower valence on titanium in $CaTi_2O_4$.

To confirm the titanium valence in $NaTi_2O_4$ and $CaTi_2O_4$, we measured XANES data at the Ti K-edge. Titanium K-edge XANES has previously been used to study titanium coordination in a variety of oxide materials, including glasses and melts as well as crystalline solids. For the majority of these studies, the materials contain titanium in the oxidation state $+4$ [15]. There are, in contrast, only a few reported studies of reduced valence in materials using Ti K-edge XANES. Of particular note are the works of Durmeyer et al. [16] and Ra et al. [17], who both studied $Li_{1+x}Ti_{2-x}O_4$ (the former study included $MgTi_2O_4$ and $TiO_2$ as reference compounds), and of Luca et al. [18] who studied lithium intercalation compounds of anatase. In all cases, distinct trends in the form of the XANES signal with average titanium oxidation state were noted, and broadly similar results were seen in each study. Unfortunately, consistent notation was not used between these studies to label the spectral features. Also, for some spectral features, there is no unanimity regarding peak assignments. Calculation of any XANES spectrum and the determination of quantitative information is difficult, particularly due to the effects of multiple scattering from the EXAFS part of the immediate post-edge region. We will therefore use the XANES as a fingerprint of oxidation state and compare our data with those previously reported, using the labeling scheme of Luca et al. [18], which is largely consistent with that adopted by the studies of titanium coordination. This will allow us to identify salient features of the spectra of $NaTi_2O_4$ and $CaTi_2O_4$, which we report for the first time.

Before discussing the subtle pre-edge features, it can be seen immediately in Fig. 2 that the position of the edge region is shifted to lower energy with decreasing titanium oxidation state. All spectra are also shifted to higher energy than the reference titanium foil, which is as expected for materials containing oxidized titanium. The edge position can be defined in a number of ways, but for a simple quantification we define the edge as the value of energy when the normalized absorption equals 0.5; edge positions are collected in Table 1. We see a clear trend with the absorption edge of the mixed-valence $NaTi_2O_4$ taking a value close to the average of the values of $TiO_2$ (anatase polymorph) and any of the three $Ti^{3+}$-containing materials, $CaTi_2O_4$, $MgTi_2O_4$ and $Ti_2O_3$. This is unequivocal evidence that the ternary oxides contain titanium with the expected valences. The features seen in the immediate post-edge region have been assigned as arising from $1s \rightarrow 4p$ and $1s \rightarrow np$ ($n > 4$) transitions. Our data from $TiO_2$ both in the pre- and post-edge regions are essentially the same as those published by Luca et al. [18].

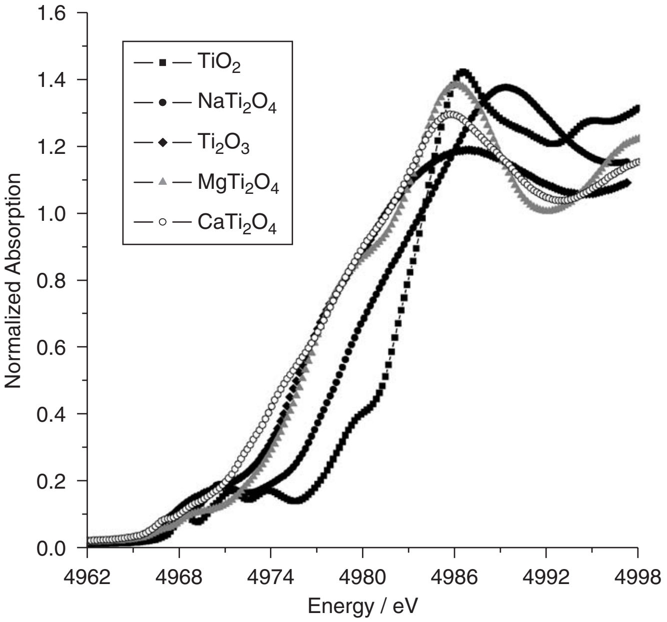

Fig. 2. Normalized titanium K-edge XANES spectra for $NaTi_2O_4$ (shown in black circles) and $CaTi_2O_4$ (shown in open circles) along with data for $Ti_2O_3$ (shown in black diamonds), $MgTi_2O_4$ (shown in gray triangles), and $TiO_2$ (shown in black squares) for comparison.

Table 1
Energies of the spectral features of the titanium K-edge XANES.

| Compound | Edge position[a] (eV) | A1 (eV) | A2 (eV) | A3 (eV) | B (eV) |
|---|---|---|---|---|---|
| $TiO_2$ | 4981.48 | 4968.32 | 4970.30 | 4971.41 | 4974.01 |
| $NaTi_2O_4$ | 4978.26 | 4968.54 | — | 4970.90 | — |
| $CaTi_2O_4$ | 4975.06 | 4967.15 | — | 4969.17 | — |
| $MgTi_2O_4$ | 4976.06 | 4967.01 | — | 4969.21 | — |
| $Ti_2O_3$ | 4975.48 | 4967.46 | — | 4968.78 | — |

The labeling notation is modeled after that used by Luca et al. (Ref. [18]).

[a] Defined as the energy at which normalized absorption equals 0.5 (see text).

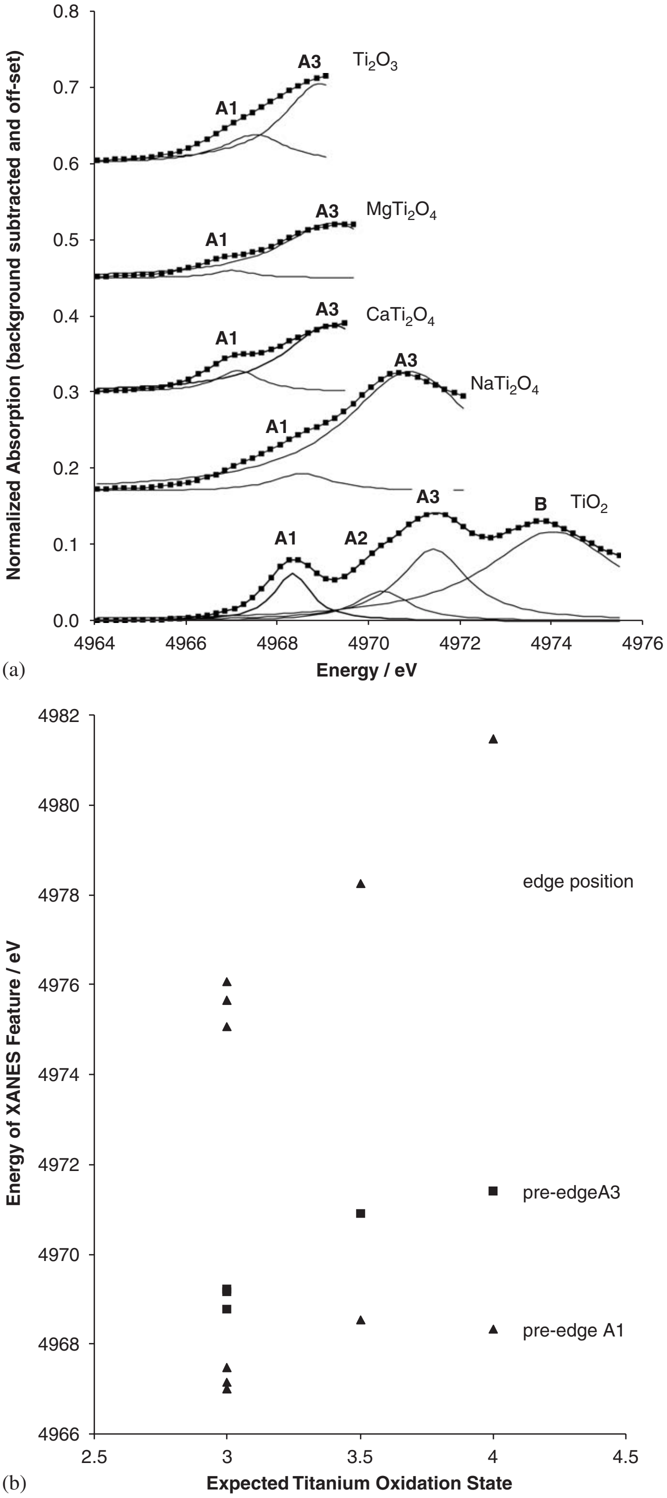

Fig. 3. (a) The pre-edge region of the XANES spectra after removal of an arctan background, along with fitted Lorentzians (lines), and (b) the energy values of features of the XANES spectra plotted against expected titanium oxidation state.

As indicated in Fig. 2 and more clearly in Fig. 3a, the Ti K-edge of each material exhibits a distinct pre-edge structure: a group of features that have been ascribed previously to dipole forbidden transitions of core 1*s* electrons to 3*d*–4*p* hybridized states [17,18]. The intensity of these features depends upon the nature of the valence band of the material studied [17]. In general it may be observed that for the materials containing titanium in oxidation states lower than +4, the pre-edge features have much less intensity and fewer are seen than for $TiO_2$, where three distinct signals are seen, A1, A3 and B, as well as a weak shoulder A2. We have used the method of Durmeyer et al. to display these features in Fig. 3a, subtracting an arctan background to simulate the edge ramp in the pre-edge region [16]. In addition, we have fitted the pre-edge spectral features as a series of Lorentzian functions in order to provide further quantification of the relationship between oxidation state and XANES spectral features. The fitted energy values for all materials are presented in Table 1 and plotted in Fig. 3b against expected oxidation state. Also plotted is the edge position defined above, and we see a distinct trend of decreasing spectral feature position with oxidation state, most pronounced for the edge position. The fitted values for $TiO_2$ show excellent agreement with those reported by Luca et al. who also studied the anatase polymorph [18]. The precise energy values vary between reported studies of $TiO_2$, probably due to miscalibration in some cases, but since we have recorded data simultaneously from a titanium foil reference we are confident that the shifts in energy between the spectra of our materials are accurate.

Durmeyer et al. noted that upon reduction of titanium to mixed-valence states between +3 and +4, the pre-edge feature we have labeled A3 becomes considerably more intense (albeit broadened) relative to A1 and B, and in some cases, such as $LiTi_2O_4$, is the only peak seen in this region of the spectrum [16]. Although the assignment of the A1 feature is controversial, most authors agree that the features we have labeled A3 and B are related to the octahedral crystal field splitting of the 3*d* orbitals: The A3 peak corresponds to the $1s \rightarrow 3d$ $t_{2g}$ transition and the B peak to the $1s \rightarrow 3d$ $e_g$ transition [16,17]. It should be noted that the feature B, if present in reduced species, is likely to be obscured by the absorption ramp, which shifts more markedly to lower energy with decreasing titanium oxidation state. In our new XANES data for $NaTi_2O_4$, one strong signal is seen in the pre-edge region, which we tentatively assign as the A3 $1s \rightarrow 3d$ $t_{2g}$ feature with only a slight low energy shoulder, resembling the spectra reported for $LiTi_2O_4$ [17] and also the lithium intercalates of anatase, where the material $Li_{0.56}TiO_2$ exhibits a remarkably similar spectrum [18]. This is consistent with the mixed-valence of titanium in $NaTi_2O_4$. The shoulder A2 seen in $TiO_2$ is no longer visible in these spectra, which is not surprising since at least one group attributed this peak, observed in anatase nanocrystals, to five-coordinate surface titanium sites with an intensity strongly correlated to particle size [19].

Upon lowering the titanium valence further to +3, Durmeyer et al. reported that in $MgTi_2O_4$, the feature A1 reappears (and not B), but is shifted to lower energy, and so two distinct pre-edge features may then be observed. [16] Our XANES data are consistent, and in the spectra for both $MgTi_2O_4$ and $CaTi_2O_4$, the A1 and A3 peaks are more clearly resolved than in the $NaTi_2O_4$ spectrum. In the case of $Ti_2O_3$, the pre-edge region is less well defined, although two features at similar energies to the other $Ti^{3+}$ materials can just be distinguished. As discussed below, the band structure calculations indicate a distinct splitting of the 3*d* $t_{2g}/e_g$ energy levels in $NaTi_2O_4$ but not in $CaTi_2O_4$. Unfortunately, due to the shifting absorption edge and the absence of the pre-edge peak B, the XANES data could not be related to the predictions from the band structure calculations. However, what is significant in the comparison of the $NaTi_2O_4$ and $CaTi_2O_4$ pre-edge features is the relative intensity of the A3 peak. Strictly speaking, the $1s \rightarrow 3d$ $t_{2g}$ transition is dipole forbidden, however hybridization of the titanium 3*d* orbitals with oxygen 2*p* orbitals relaxes the selection rule. Consistent with the interpretation of Ra et al. [17], the higher oxidation state of Ti in $NaTi_2O_4$ as compared to $CaTi_2O_4$, lowers the energies of the Ti 3*d* orbitals, allowing for more effective hybridization with the oxygen 2*p* orbitals and more intensity in the A3 peak. Interestingly, the XANES of mixed-valence $NaTi_2O_4$ cannot be simulated as a 50–50 mixture of the signal for $TiO_2$ and $MgTi_2O_4$, and this is particularly clear by the absence of the pre-edge peak B. This is consistent with the absence of two distinct titanium sites, one for $Ti^{3+}$ and one for $Ti^{4+}$, in $NaTi_2O_4$.

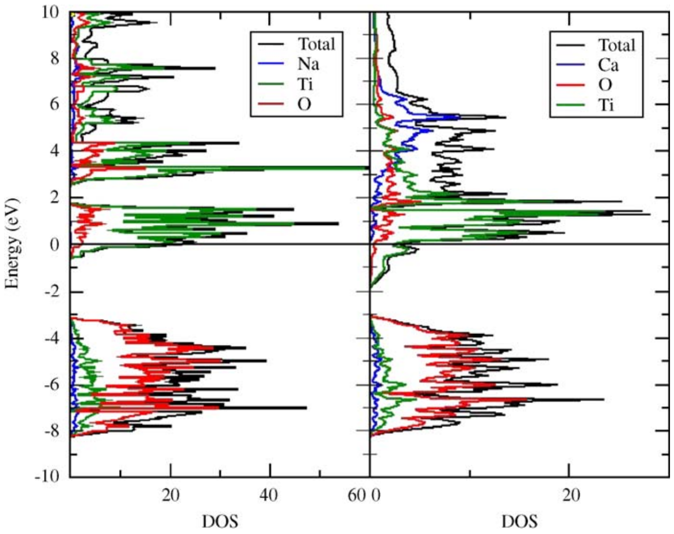

Fig. 4. (a) On the left, the electronic density of states (shown in black) as calculated for $NaTi_2O_4$. Partial density of states curves for sodium, titanium, and oxygen contributions are shown in blue, green and red, respectively. (b) On the right, the electronic density of states (shown in black) as calculated for $CaTi_2O_4$. Partial density of states curves for calcium, titanium, and oxygen contributions are shown in blue, green and red, respectively.

### 3.2. Electronic band structure of $NaTi_2O_4$

The electronic density of states calculated for $NaTi_2O_4$ is shown in Fig. 4a with titanium and oxygen contributions shown in green and red, respectively. The valence band in this material, covering the energy range from −8.3 to −3.2 eV, is predominantly oxygen *2p* in character. Titanium orbital contributions dominate in the region near the Fermi level. The conduction band is split into two distinct bands by the pseudo-octahedral coordination around titanium, corresponding to the characteristic $t_{2g}/e_g$ splitting of the Ti *3d* orbitals.[1] The lower conduction band (−0.6 to +1.7 eV) contains 24 bands (3 per Ti atom) and arises from the $\pi^*$ interaction between the Ti *3d* $t_{2g}$ orbitals and oxygen, while the upper conduction band (+2.4 to +4.3 eV) contains 16 bands (2 per Ti atom) and originates

---

[1] The symmetry descriptors $t_{2g}$ and $e_g$ are only strictly valid for ideal octahedral site symmetry. While the symmetry is lower in these compounds the local octahedral environment is approximately maintained.

from the $\sigma^*$ interaction between the Ti $3d$ $e_g$ orbitals and oxygen. The Fermi level cuts the Ti $3d$ $t_{2g}$–O $2p$ $\pi^*$ bands, consistent with the mixed-valence ($Ti^{3.5+}$) and partial occupancy ($d^1/d^0$) of the Ti $3d$ orbitals.

The $E$ vs. $k$ plot (Fig. 5) shows the complete band dispersion of the 24 bands that belong to the Ti $3d$ $t_{2g}$–O $2p$ $\pi^*$ set. As implied by the DOS plot, the Ti $3d$ bands show relatively little dispersion. However, it is interesting to compare the differences in band dispersion along the $\Gamma$(G)–X, $\Gamma$(G)–Y and $\Gamma$(G)–Z directions. There is almost no dispersion in the first two directions, whereas there is a moderate degree of dispersion along the $\Gamma$(G)–Z direction. This direction is parallel to the direction along which the edge-sharing double rutile-type chains run. Thus the electron transport that occurs in this compound is expected to take place within the double rutile-type chains. A simplistic reading of the density of states diagram suggests that $NaTi_2O_4$ should be metallic, based on the fact that the Fermi level cuts through a number of bands. However, given the narrow width of the conduction bands, localized electrons and activated electron transport would be a more realistic interpretation.

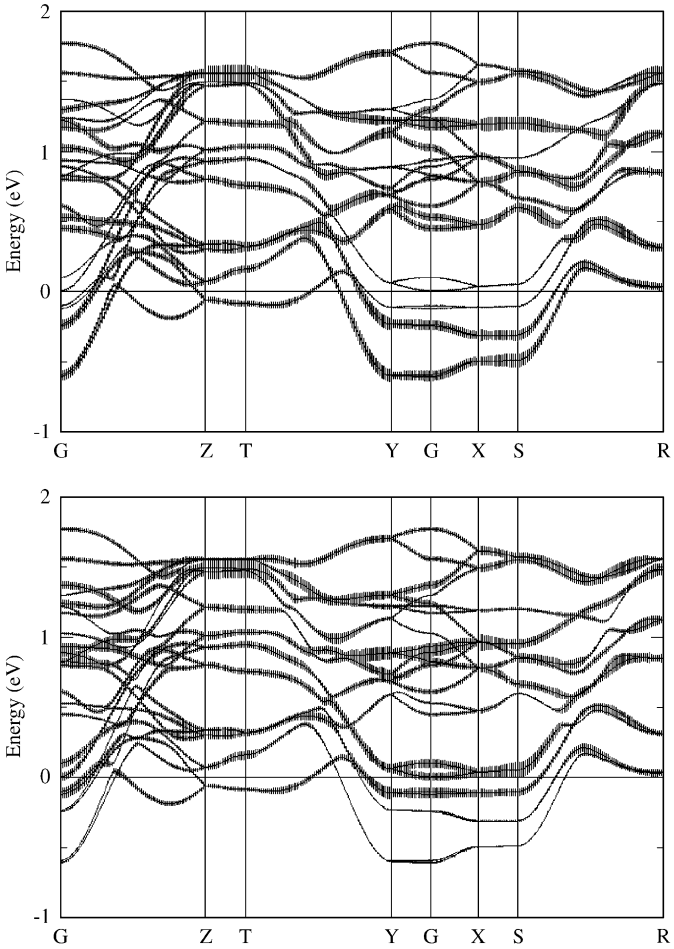

Fig. 5. The $E$ vs. $k$ diagrams for the conduction bands as calculated for $NaTi_2O_4$. (a) In the top figure, the orbital contributions for the $3d$ orbitals on Ti(1) are indicated by the fatband hatching. (b) Similarly, the contributions of $3d$ orbitals on Ti(2) are shown in the bottom figure.

Along the $Y$–$\Gamma$(G), $\Gamma$(G)–X, and X–S directions, where the bands are particularly flat, it is possible to identify four pairs of bands, eight bands in total (one for each titanium atom in the unit cell), that lie below the others. These bands are the primary ones that traverse the Fermi level, so they will be of particular importance for the transport properties. They also account for almost all of the occupied states in the conduction band region. Comparison of the Ti(1) and Ti(2) $3d$ fatband plots, emphasized in Figs. 5a and 5b respectively, reveals that the four bands with Ti(1) parentage lie below the four bands with Ti(2) parentage. In the above mentioned regions of reciprocal space, six of the eight bands lie below the Fermi energy; four of these six bands are clearly associated with $3d$ orbitals on Ti(1), suggesting a partial charge ordering. To investigate the extent of charge-ordering, the Mulliken orbital populations of the Ti $3d$ orbitals were examined. The $d$-orbital population of the Ti(1) atom was found to be 1.96 electrons per Ti, while for Ti(2) the population was 1.83 electrons per Ti. These values cannot be compared with expectations based on a literal interpretation of oxidation states, which would yield 0 and 1 electrons per atom for $Ti^{4+}$ and $Ti^{3+}$, respectively, because the Ti–O bonds have considerable amount of covalent character. In order to calibrate these numbers, the Mulliken orbital populations were examined for two compounds where the titanium oxidation state was unambiguous, $TiO_2$ (rutile) and $CaTi_2O_4$. The Ti $3d$ orbital population was 1.70 electrons per titanium for rutile, while for $CaTi_2O_4$ it was 2.02 electrons per titanium. The fact that both Ti atoms have orbital populations that are intermediate between $Ti^{4+}$ and $Ti^{3+}$ is consistent with the XANES data. However, the computations do suggest a preferential occupation of the Ti(1) $3d$ orbitals. While this preference falls short of complete charge ordering, it does help to explain the observation that the Ti(1) centered octahedra are both more distorted and have a larger average Ti–O distance than do the Ti(2) centered octahedra. Formally, we might represent this charge segregation as $NaTi(1)^{3.5-\delta}Ti(2)^{3.5+\delta}O_4$.

Structural evidence for preferential occupation of the Ti(1) site can also be extracted from a more detailed analysis of oxygen–oxygen separations along the rutile-type chains. Fig. 6 compares the relevant O–O distances within the Ti(1) chains to those in the Ti(2) chains as well as to the O–O distances found in the rutile form of $TiO_2$. In rutile, the O–O distance across the shared edge is 2.54 Å, while the O–O distance along the edge that is parallel to the chain direction is 2.96 Å. The accepted wisdom is that adjacent oxygens across the shared edge move closer together in order to shield the $Ti^{4+}$ ions from each other. In the Ti(2) chains of $NaTi_2O_4$, we find the same O–O distance along the edge parallel to the chain direction, 2.96 Å, but compared to rutile, a slightly longer O–O distance is observed across the shared edge, 2.69 Å. In the Ti(1) chain, the O–O distance across the shared edge has opened up considerably to 2.84 Å. These structural features

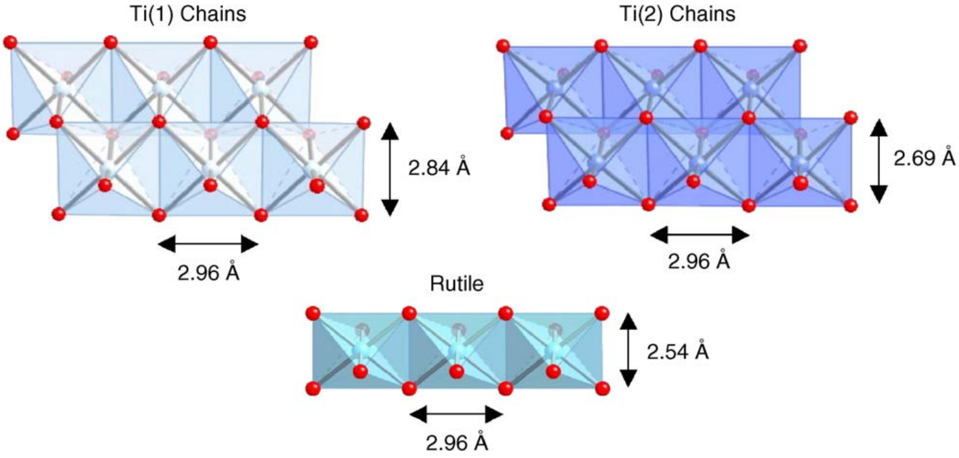

Fig. 6. Oxygen–oxygen distances along the two different rutile-type chains found in $NaTi_2O_4$ compared with the O–O distances in the chain found in the rutile form of $TiO_2$.

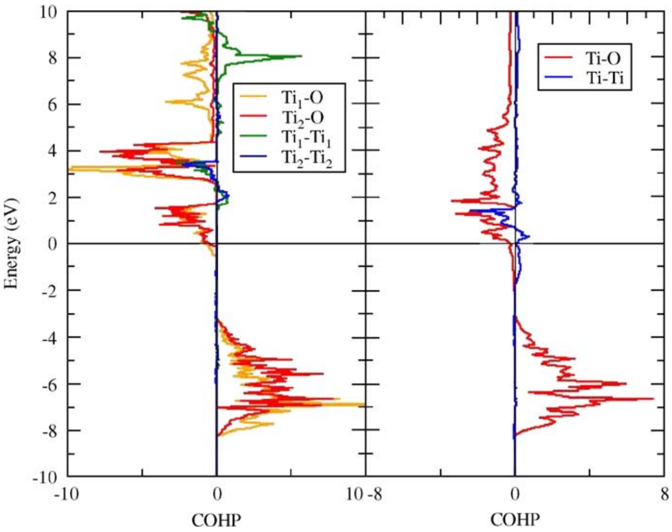

Fig. 7. (a) On the left, cooperative overlap Hamiltonian population (COHP) plots calculated for $NaTi_2O_4$. A positive COHP value indicates a bonding interaction, while a negative COHP value indicates an antibonding interaction. The Ti(1)–O interaction is shown in yellow, the Ti(2)–O interaction in red, the Ti(1)–Ti(1) interaction in green and the Ti(2)–Ti(2) interaction in blue. (b) On the right, cooperative overlap Hamiltonian population (COHP) curves for $CaTi_2O_4$ showing in red, Ti–O bonding/antibonding interactions and in blue, Ti–Ti bonding/antibonding interactions.

are consistent with the oxidation state conclusions derived from the Mulliken population analysis.

Given the presence of edge-sharing octahedra and partially occupied Ti *3d* orbitals the possibility exists that metal–metal bonding plays a role in defining the electronic structure. A useful complement to the density of states is the cooperative overlap Hamiltonian population (COHP) analysis, shown in Fig. 7a [20]. The COHP plots provide a measure of the importance of metal–metal bonding in comparison with metal–oxygen bonding. The Ti–O COHP plot shows a transition from bonding states to antibonding states as the *d*-orbitals are populated, as expected for an early transition metal oxide. On the other hand, the Ti–Ti bonding contributions become significant only well above the Fermi level, revealing that metal–metal bonding is of minimal importance. The bottom of the conduction band is exclusively Ti–O antibonding in character, which differs from other rutile-type structures containing partially filled *d*-orbitals, such as $VO_2$, $CrO_2$, and $RuO_2$, where both metal–oxygen antibonding and metal–metal bonding interactions can be found at the bottom of the conduction band [21]. This analysis is consistent with the Ti–Ti distances observed in the structure; the closest Ti–Ti distance is 2.96 Å, as discussed in more detail below.

### 3.3. Electrical and magnetic properties of $NaTi_2O_4$

The observed electrical and magnetic properties of $NaTi_2O_4$ are consistent with the results from the band structure calculations. Fig. 8a shows the two-probe electrical resistivity as a function of temperature, measured on a crystal of $NaTi_2O_4$. The extremely small size of the crystal ($0.02 \times 0.04 \times 0.62$ mm) made it impossible to mount leads for a proper four-probe measurement. Nonetheless, the data shown in Fig. 8a illustrate semiconducting behavior between 40 and 300 K. The small breaks in the data evident at 155 and 220 K were caused by self-heating of the crystal as the electrometer changed range. Below 40 K, the sample became too resistive to measure reliably. The inset shows a fit of the data from 85 to 300 K to Eq. (1), resulting in a band gap ($E_g$) of 0.2 eV.

$$\sigma = \sigma_0 e^{-E_g/2kT}. \tag{1}$$

The magnetic susceptibility of $NaTi_2O_4$ was measured from 2 to 600 K. Due to the similarity in composition to the known superconductor, $LiTi_2O_4$, we first checked the sample for superconductivity. The sample was paramagnetic at all temperatures with no evidence of superconductivity down to 2 K. Although $NaTi_2O_4$ shares the same titanium valence with $LiTi_2O_4$, the structures of the

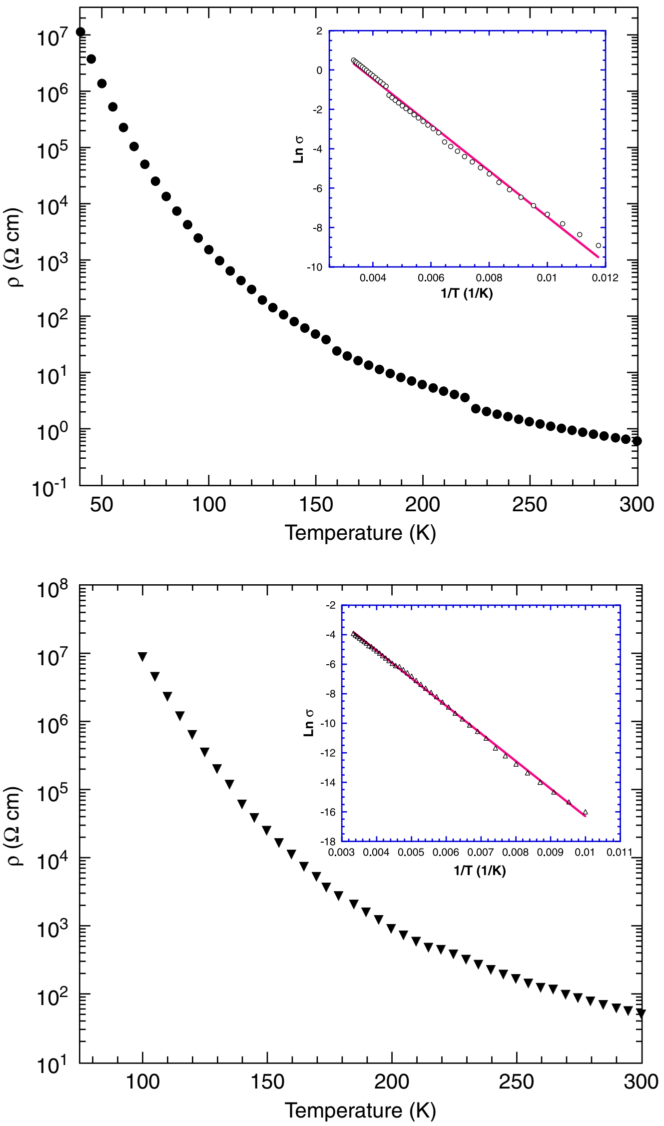

Fig. 8. (a) On the top, two-probe resistivity measurements on a crystal of $NaTi_2O_4$ (crystal dimensions, $0.02 \times 0.04 \times 0.62$ mm) as a function of temperature from 40 to 300 K. The inset plot results in an estimate of the band gap energy, $E_g = 0.2$ eV. (b) On the bottom, two-probe resistivity measurements on a crystal of $CaTi_2O_4$ (crystal dimensions, $0.04 \times 0.04 \times 0.32$ mm) as a function of temperature from 100 to 300 K. The inset plot results in an estimate of the band gap energy, $E_g = 0.3$ eV.

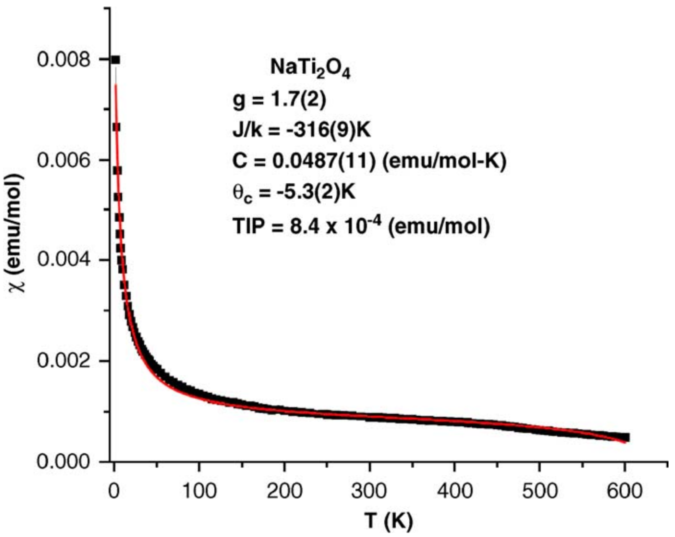

Fig. 9. Magnetic susceptibility of $NaTi_2O_4$ measured from 2 to 600 K. The solid line is a fit to the model described in the text consisting of an $S = 1/2$ linear chain model plus a Curie–Weiss and a TIP term.

two materials are radically different. Thus, it is not surprising that $NaTi_2O_4$ is not a superconductor.

Fig. 9 shows the magnetic susceptibility for $NaTi_2O_4$ from 2 to 600 K. Note the Curie tail at low temperatures and the weak maximum near 400 K. A possible interpretation of these data is to ascribe the low temperature tail to uncoupled spins and the broad maximum to short-range correlated spins. The solid line in Fig. 9 is a fit to the model in Eq. (2). This model considers three contributions to the magnetic susceptibility: The first term represents the susceptibility of an S = 1/2 linear chain to account for the correlated spins [22], and the second and third terms consist of a Curie–Weiss plus a temperature independent paramagnetic (TIP) contribution to account for the uncorrelated spins.

$$\chi_M = \left(\frac{Ng^2\mu_B}{kT}\right)\left[\frac{0.25 + 0.18297\left(\frac{J}{k}\right)^2}{1 + 1.5467\left(\frac{J}{k}\right) + 3.4443\left(\frac{J}{k}\right)^3}\right] + \frac{C}{T-\theta} + \mathrm{TIP}. \quad (2)$$

The fitted parameters are $g = 1.7(2)$, $J/k = -316(9)$ K, $C = 0.0487(11)$ emu/mol K, $\theta_c = -5.3(2)$ K and TIP $= 8.4(2) \times 10^{-4}$ emu/mol. While this is clearly a crude approximation to the real situation, the parameters are not unreasonable and are consistent with the partial charge-ordered model described above. [23] If the Ti(1) site is occupied preferentially but not fully by $Ti^{3+}$, one would expect quasi-one-dimensional spin correlations of varying finite lengths along the edge-shared double chains as well as uncorrelated spins in the Ti(2) sites. Apparently, the infinite chain approximation appears to capture the essential features. An attempt to fit the same data using an $S = 1/2$ dimer model to account for the short-range correlations was not successful.

### 3.4. Electronic band structure of $CaTi_2O_4$

The partial density of states calculated for $CaTi_2O_4$ is shown in Fig. 4b, and the $E$ vs. $k$ band structure is shown in Fig. 10. There are four titanium atoms in the unit cell, which give rise to 20 bands of Ti *3d* orbital parentage located between −2.2 and +4.0 eV. Unlike the electronic structure of $NaTi_2O_4$, there is no clear splitting of the Ti *3d* $t_{2g}$ and $e_g$ conduction bands. The lack of a gap probably results from the larger distortion of the local octahedral coordination environment around titanium in $CaTi_2O_4$. Interestingly though there are two bands split off to lower energy, residing almost completely below $E_F$. The fatband

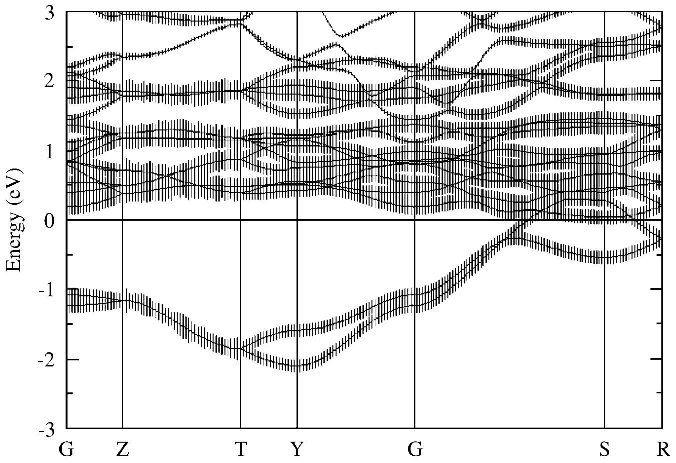

Fig. 10. The *E* vs. *k* diagrams for the conduction bands as calculated for $CaTi_2O_4$. The orbital contributions for the *3d* orbitals on Ti are indicated by the fatband hatching.

analysis reveals that these two bands are primarily of Ti $3dx^2{-}y^2$ parentage. Across most of the Brillouin zone these two bands are reasonably well separated from the rest of the conduction band and are the only bands lying below the Fermi level. There are four $Ti^{3+}$ atoms per unit cell, providing four *3d* electrons to completely fill these two bands. It is worth noting that as there are only two bands split off and four titanium atoms per unit cell, these bands do not represent a given *3d* orbital (e.g., $d_{x^2-y^2}$) on each Ti atom.

The COHP curves shown in Fig. 7b are very instructive. Unlike $NaTi_2O_4$ there is minimal Ti–O antibonding character and a significant amount of Ti–Ti bonding character in the filled conduction band states. The filling of the conduction band appears to be optimal in order to maximize Ti–Ti bonding interactions while minimizing the antibonding Ti–O interactions. The two lowest energy conduction bands are predominantly Ti–Ti bonding in character with only a minor Ti–O antibonding contribution. Given the evidence for Ti–Ti bonding the next question is whether the Ti–Ti bonding is localized, for example leading to the formation of Ti–Ti dimers, or delocalized. With four titanium atoms per unit cell it is possible to form two dimers. If this occurs there should be two Ti–Ti bonding bands below the Fermi level and two Ti–Ti antibonding bands located somewhere higher up in the conduction band. This is exactly what is seen in the *E* vs. *k* and COHP plots. As the two bands below the Fermi level are not very disperse, we would expect the Ti–Ti bonding electrons to be fairly localized.

Further support for the assertion that Ti–Ti dimers form in $CaTi_2O_4$ (at room temperature) can be found in the details of the crystal structure. Ti–Ti distances within a given double rutile-type chains are 3.135(1) and 3.140(2) Å. This distance is longer than the Ti–Ti distance in rutile or $NaTi_2O_4$. However, the distance between titanium atoms in neighboring double rutile-type chains within a puckered sheet is 2.784(1) Å. The very long O–O distance across this shared octahedral edge, 3.14 Å, facilitates the Ti–Ti interaction. The metal–metal distance in $CaTi_2O_4$ is shorter than the shortest Ti–Ti distances in both Ti metal (2.896 Å) and the low-temperature structure of $MgTi_2O_4$ (2.853(7) Å), where dimerization has been documented [6]. The short interchain Ti–Ti distance in $CaTi_2O_4$ signifies considerable Ti–Ti bonding between neighboring rutile-type chains. We propose that this dimerization is the driving force for the change in structural topology upon going from $NaTi_2O_4$ to $CaTi_2O_4$. In particular, it can now be understood why $CaTi_2O_4$ violates Pauling's rules and adopts a structure involving more edge-sharing than necessitated by the stoichiometry [24].

### *3.5. Electrical and magnetic properties of $CaTi_2O_4$*

The formation of localized Ti–Ti dimers at room temperature in $CaTi_2O_4$ should make this compound both diamagnetic and semiconducting. The two-probe electrical resistivity data are shown in Fig. 8b, as measured on a small crystal (0.04 × 0.04 × 0.32 mm) of $CaTi_2O_4$. The increasing resistivity with decreasing temperature is consistent with semiconducting behavior for this material. Below 100 K, the crystal was too resistive to measure reliably. The fit of the data to Eq. (1), as shown in the inset to Fig. 8b, results in an estimate of 0.3 eV for the band gap energy over this temperature range. The resistivity values and the resulting band gap energy are consistently higher than the corresponding values determined from $NaTi_2O_4$ crystals.

The magnetic susceptibility of $CaTi_2O_4$ as a function of temperature from 5 to 800 K is plotted in Fig. 11. First, the susceptibility for $CaTi_2O_4$ is significantly lower than that for $NaTi_2O_4$ by about a factor of two over most of the measured temperature range in spite of the higher concentration (2 ×) of $Ti^{3+}$ spins. The low-temperature data, 5 to 75 K were fit to a Curie–Weiss plus a

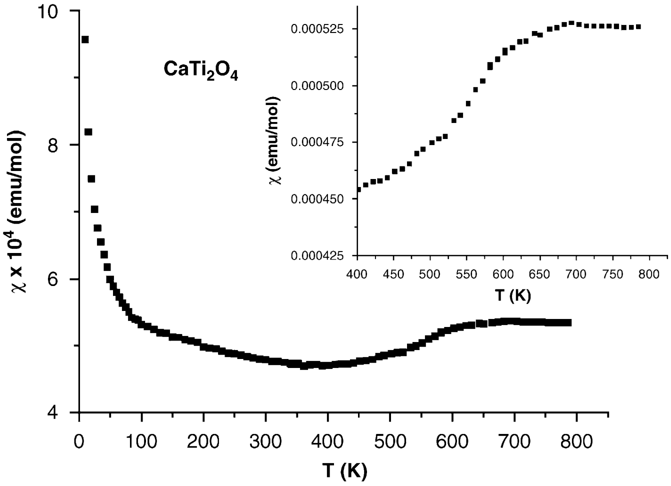

Fig. 11. Magnetic susceptibility of $CaTi_2O_4$ measured from 5 to 800 K. The inset shows the high-temperature region expanded to illustrate the rise in susceptibility above 500 K.

temperature-independent term yielding the results $C = 0.0056(2)$ emu/mol K, $\theta_c = -1.8(2)$ K and TIP $= 4.9(1) \times 10^{-4}$ emu/mol. The Curie constant indicates a very low concentration of unpaired $Ti^{3+}$ ions, less than 1%, assuming $S = 1/2$ spins. Subtraction of the Curie–Weiss tail results in a nearly temperature independent susceptibility of value $\chi \sim 4.5 \times 10^{-4}$ emu/mol from 5 to 450 K. The inset shows a significant increase in the susceptibility to $5.3 \times 10^{-4}$ emu/mol over the range 450–600 K, which then remains temperature independent to near 800 K. The TIP behavior over the low temperature regime could be interpreted either as a Pauli susceptibility from a partially filled *d*-band or a van Vleck-type contribution from low lying states above a spin singlet ground state. Taking the two probe resistivity data of Fig. 8b at face value, the latter interpretation is more consistent. The susceptibility increase at high temperature may be due to an insulator to metal transition as seen in $MgTi_2O_4$ [5] or a structural phase transition. The available data do not permit a conclusion on this issue. We are currently pursuing high-temperature diffraction studies to seek further evidence.

## 4. Conclusions

We have reported for the first time, the properties of $NaTi_2O_4$ and $CaTi_2O_4$. Results from XANES at the Ti K-edge including the edge position and pre-edge spectral features all confirm the presence of mixed-valence titanium ($Ti^{3.5+}$) in $NaTi_2O_4$ and $Ti^{3+}$ in $CaTi_2O_4$. Band structure calculations indicate minimal Ti–Ti bonding in $NaTi_2O_4$, and instead, suggest a partial charge segregation of the electron density to one of the two titanium sites. These results are consistent with the observed transport properties of a small band-gap semiconductor and data from temperature dependent magnetic susceptibility studies indicating a disordered system of spins. In contrast, band structure calculations for $CaTi_2O_4$ clearly show Ti–Ti bonding and formation of dimers in this material. From a study of Ti–Ti distances, we conclude that these Ti–Ti dimers form between titanium atoms in neighboring double rutile-type chains rather than between atoms in the same chain. Since this close inter-chain distance is not observed in the $NaTi_2O_4$ structure (calcium ferrite-type), the dimerization offers an explanation for the change in structure for $CaTi_2O_4$. Electrical resistivity studies of $CaTi_2O_4$ are consistent with weak dimerization at and below room temperature; we observed semiconducting behavior with higher resistivities and a slightly larger band gap as compared to $NaTi_2O_4$. Magnetic susceptibility data for $NaTi_2O_4$ were interpreted in terms of a partial charge ordering involving both one-dimensional short-range spin correlations and paramagnetic contributions. For $CaTi_2O_4$ the susceptibility is smaller by almost an order of magnitude, which is consistent with the formation of Ti–Ti dimers. After subtraction of a very weak Curie–Weiss low-temperature tail, the susceptibility that was observed consisted of a temperature-independent (TIP) regime from 5 to 400 K followed by a gradual increase of about 20% to a second TIP plateau from 600 to 800 K. The existing data do not permit a unique interpretation of these data, but an insulator to metal transition at high temperatures is possible. Although neither $NaTi_2O_4$ nor $CaTi_2O_4$ exhibits superconductivity, these materials nonetheless offer an opportunity to extend our understanding of structure property relationships in the $ATi_2O_4$ family of reduced titanates.

## Acknowledgments

We thank the CCLRC for providing beamtime at the Daresbury SRS, Christopher Wright for assistance with measuring some of the XANES data, and Prof. Sang-Wook Cheong, Department of Physics and Astronomy, Rutgers University for kindly supplying the sample of $MgTi_2O_4$. M.J.G. thanks NSF-CAREER (DMR-9733329) and a William and Flora Hewlett Foundation Award of Research Corporation (Award C-3488) for financial support, Peter Klavins in the Department of Physics at the University of California Davis for assistance with the electrical resistivity measurements, and Prof. John Essick, Department of Physics, Reed College for advice and experimental assistance. J.E.G. thanks the Natural Science and Engineering Research Council of Canada for a Discovery Grant. M.W.S., H.W.E. and P.M.W. thank Prof. O.K. Andersen and Dr. O. Jepsen, Max Planck Institute, Stuttgart for providing the LMTO code, Prof. Ram Seshadri, Materials Research Laboratory, UC-Santa Barbara for assistance with the calculations, as well as the National Science Foundation (DMR-0094271), and the Sloan Foundation for support.

## References

[1] [a] See for example L. Brohan, R. Marchand, M. Tournoux, J. Solid State Chem. 72 (1988) 145–153;
[b] M. Evain, M.-H. Whangbo, L. Brohan, R. Marchand, Inorg. Chem. 29 (1990) 1413–1416;
[c] S.J. Clarke, A.J. Fowkes, A. Harrison, R.M. Ibberson, M.J. Rosseinsky, Chem. Mater. 10 (1998) 372–384.

[2] [a] D.C. Johnston, H. Prakash, W.H. Zachariasen, R. Viswanathan, Mater. Res. Bull. 8 (1973) 777–784;
[b] D.C. Johnston, J. Low Temp. Phys. 25 (1976) 145–175.

[3] P.M. Lambert, M.R. Harrison, P.P. Edwards, J. Solid State Chem. 75 (1988) 332–346.

[4] H. Hohl, C. Kloc, E. Bucher, J. Solid State Chem. 125 (1996) 216–223.

[5] M. Isobe, Y. Ueda, J. Phys. Soc. Jpn. 71 (2002) 1848–1851.

[6] M. Schmidt, W. Ratcliff II, P.G. Radaelli, K. Refson, N.M. Harrison, S.W. Cheong, Phys. Rev. Lett. 92 (2004) 056402.

[7] H.D. Zhou, J.B. Goodenough, Phys. Rev. B 72 (2005) 045118.

[8] J. Akimoto, H. Takei, J. Solid State Chem. 79 (1989) 212–217.

[9] [a] E.F. Bertaut, P. Blum, Acta Crystallogr. 9 (1956) 121–126;
[b] M.P. Rogge, J.H. Caldwell, D.R. Ingram, C.E. Green, M.J. Geselbracht, T. Siegrist, J. Solid State Chem. 141 (1998) 338–342.

[10] M.J. Geselbracht, L.D. Noailles, L.T. Ngo, J.H. Pikul, R.I. Walton, E.S. Cowell, F. Millange, D. O'Hare, Chem. Mater. 16 (2004) 1153–1159.

[11] N. Binsted, J.W. Campbell, S.J. Gurman, P.C. Stephenson, EXAFS Data Analysis Program, Daresbury Laboratory, 1991.
[12] O.K. Andersen, Phys. Rev. B 12 (1975) 3060–3083.
[13] O.K. Andersen, O. Jepsen, Phys. Rev. Lett. 53 (1984) 2571–2574.
[14] J.P. Perdew, Y. Wang, Phys. Rev. B 33 (1986) 8800–8802.
[15] [a] See for example F. Farges, G.E. Brown, J.J. Rehr, Phys. Rev. B 56 (1997) 1809–1819;
  [b] G. Mountjoy, D.M. Pickup, G.W. Wallidge, R. Anderson, J.M. Cole, R.J. Newport, M.E. Smith, Chem. Mater. 11 (1999) 1253–1258.
[16] O. Durmeyer, J.P. Kappler, E. Beaurepaire, J.M. Heintz, M. Drollin, J. Phys: Condens. Matter 2 (1990) 6127–6136.
[17] W. Ra, M. Nakayama, H. Ikuta, Y. Uchimoto, M. Wakihara, Appl. Phys. Lett. 84 (2004) 4364–4366.
[18] V. Luca, T.L. Hanley, N.K. Roberts, R.F. Howe, Chem. Mater. 11 (1999) 2089–2102.
[19] V. Luca, S. Djajanti, R.F. Howe, J. Phys. Chem. B 102 (1998) 10650–10657.
[20] R. Dronskowsi, P.E. Blochl, J. Phys. Chem. 97 (1993) 8617–8624.
[21] [a] J.K. Burdett, Acta Crystallogr. B 51 (1995) 547–558;
  [b] P.I. Sorantin, K. Schwarz, Inorg. Chem. 31 (1992) 567–576.
[22] W. Hiller, J. Strahle, A. Datz, M. Hanack, W.E. Hatfield, L.W. ter Haar, P. Gutlich, J. Am. Chem. Soc. 106 (1984) 329–335.
[23] [a] For other examples of partial charge ordering in oxides see J.R. Cullen, Philos. Mag. B 42 (1980) 387–391;
  [b] J.E. Greedan, C.R. Wiebe, A.S. Willis, J.R. Stewart, Phys. Rev. B 65 (2002) 184424;
  [c] J.L. Gavilano, D. Rau, B. Pedrini, K. Magishi, M. Weller, J. Hinderer, H.R. Ott, S.M. Kazakov, J. Karpinski, Phys. B 359–561 (2005) 1237–1239.
[24] L. Pauling, J. Am. Chem. Soc. 51 (1929) 1010–1026.